



Influence of non-steady transient heat flux on flow boiling heat transfer and pressure drop in horizontal pipes

W.J. Van den Bergh¹, J. Dirker¹, C.N. Markides^{2,3}, J.P. Meyer^{1,*}

¹ Department of Mechanical and Aeronautical Engineering, University of Pretoria, Pretoria, South Africa

² Clean Energy Processes (CEP) Laboratory, Department of Chemical Engineering, Imperial College London, London, UK

³ Kutateladze Institute of Thermophysics, Novosibirsk, Russian Federation

ARTICLE INFO

Article history:

Received 23 May 2021

Revised 14 August 2021

Accepted 1 September 2021

Available online 20 September 2021

Keywords:

concentrated solar power

cooling

direct steam generation

flow boiling

heat flux

heat transfer

pressure drop

transient

ABSTRACT

Transient heat fluxes imposed on solid surfaces can significantly affect the heat transfer and pressure drop of flow boiling processes in diverse fields ranging from microprocessor electronics cooling to waste-heat recovery and large-scale direct steam generation in concentrated solar applications. A series of simulated transients were applied in this experimental study to investigate the saturated flow boiling of R-245fa in a horizontal pipe. The test section consisted of an 8.31 mm inner diameter, 800 mm long heated pipe. The imposed transient conditions involved spatially uniform but temporally varying heat fluxes imposed on the pipe. A baseline condition with a saturation temperature of 35°C, a heat flux of 7.5 kW/m² and a mass flux of 200 kg/m²s was considered over a vapour quality range from 0.10 to 0.85. Motivated by direct steam generation application case studies and based on actual solar direct normal irradiation data, reductions with an amplitude of 75% of the baseline heat flux were imposed over a period of 30 s. The waveform types were step, triangular and sinusoidal pulses, and were applied in a controlled fashion. It was found that during the step perturbation, the heat transfer coefficient was approximately 30% lower than the steady state condition. The triangular and sinusoidal perturbations resulted in heat transfer coefficients that were 8% lower than that of the steady state. The pressure gradient through the test section was unaffected by the imposed perturbations.

© 2021 The Authors. Published by Elsevier Ltd.

This is an open access article under the CC BY license (<http://creativecommons.org/licenses/by/4.0/>)

1. Introduction

Concentrated solar power (CSP) is one of the most attractive options for decoupling electricity generation and heating from conventional technologies based on fossil fuels. Many studies have been performed to investigate the suitability of CSP for desalination of water [1, 2], process heating [3], combined heat and power [4], and distributed power generation [5]. Although it was first used for power generation in the early 1900s [6], it has lately received renewed attention [7–9]. In CSP systems, direct normal irradiation (DNI, the portion of sunlight that is perpendicular to the surface of the earth), is optically focused onto a collector pipe carrying a fluid. The fluid is heated for use in a process application or as part of a thermodynamic energy conversion cycle. Several techniques exist, including the utilization of linear solar focusing onto horizontal pipes via, for instance, parabolic trough reflectors. This focal method is attractive because it only requires

a simple one-dimensional solar tracking system, is highly affordable and scalable, and has been commercially viable for over a century [10].

Several CSP plants are already in commercial operation. This includes systems that use thermodynamic cycles such as the Stirling or Rankine cycles [11]. Each cycle type operates on different working fluids and have different associated advantages and disadvantages.

Rankine cycles, that operate with water/steam in the liquid, two-phase and vapour regions are commonly used with CSP. The collected solar heat is used to produce high pressure superheated steam to drive steam turbines. Typically, an intermediate heat transfer fluid, such as molten salts, are heated in the solar field and used to produce the steam via a heat exchanger. When the working fluid is heated directly into steam within the solar field, without the use of the intermediate heat exchanger, the process is referred to as direct steam generation (DSG). The main advantages of this direct heating approach are the inherent reduced complexity of the system architecture [12], reduced thermodynamic losses, and the possible alleviation of the relatively low temperature limit imposed

* Corresponding Author.

E-mail address: josua.meyer@up.ac.za (J.P. Meyer).

Nomenclature

A	Area [m ²]
Bi	Biot number [-]
c_p	Isobaric specific heat capacity [J/kgK]
d	Diameter [m]
EB	Energy balance error [-]
G	Mass flux [kg/m ² s]
h	Specific enthalpy [J/kg]
I	Electric current [A]
k	Thermal conductivity [W/mK]
L	Length [m]
m	Mass [kg]
\dot{m}	Mass flow rate [kg/s]
p	Pressure [Pa]
\dot{q}	Heat flux [W/m ²]
\dot{Q}	Heat transfer rate [W]
t	Time [s]
T	Temperature [K, °C]
V	Electric voltage [V]
V	Volume [m ³]
x	Vapour quality [-]

Special characters

α	Heat transfer coefficient [W/m ² K]
ε	Void fraction [-]
ρ	Density [kg/m ³]
σ	Surface tension [N/m]

Subscripts

c	Cross-sectional
C	Characteristic
cond	Condenser
Cu	Copper
f	Saturated liquid
frict	Friction
g	Saturated vapour
h	Heated
i	Inner
in	Inlet
mom	Momentum
o	Outer
out	Outlet
pre	Preheater
ref	Refrigerant
s	Surface
sat	Saturation
static	Static
test	Test section
w	Water
wall	Pipe wall

ciencies of 7% [19], with actual experimental ORC systems demonstrating an average cycle efficiency of 5% [20]. ORC systems employing R-245fa have been investigated particularly in the context of small-scale, low-temperature generation applications, with a modified ORC system being proposed for temperatures below 80°C [21]. Additionally, R-245fa ORC systems have been studied for waste-heat recovery in heavy-duty diesel engines [22, 23] and for combination with high-concentration solar photovoltaics (PV) [24]. Some of the other applications of relevance to R-245fa include microelectronic chip electronics cooling [25], and battery cooling systems in, for instance, electric vehicles. In all of these applications flow boiling of the fluid is either a necessity or beneficial to the intended process.

Regardless of the application, temporal variations in the imposed heat flux can be expected. In solar systems operating with DSG in particular, heat flux variations are directly linked to changes in the DNI which, for example, can be caused by temporary cloud coverage [26]. This could potentially be problematic in such systems in which the fluid has to be superheated before delivery to a turbine or directly to an end-user. To ensure stable and reliable performance, the correct design and operation of the solar field is important. Thus far, studies that focused on the effect of a decrease and increase in the flow boiling heat flux on the heat transfer coefficient in the collector pipes have been limited.

Ait Lahoussine Ouali et al. [27] found that cloud coverage had a significant impact on the simulated gross power output of a proposed CSP plant in Morocco. Feldhoff and Hirsch [28] noted that the current annual DNI yield predictions relied on steady-state heat balances and did not take into account short-term variations caused by cloud coverage. Eck and Hirsch [29] developed a transient simulation tool to model the impact of cloud shading and found that following a cloud disturbance on a section of the parabolic trough, a significant amount of time was needed for the system to reach steady state. The orientation of the field was also of particular importance.

Wang et al. [30] constructed a test section incorporating non-uniform heat flux to simulate better the heat flux distribution on the collector pipe of an actual parabolic trough. Using R-245fa as fluid, they found that the non-uniformity of the heat flux enhanced nucleation boiling, and that the transition to the fully annular flow pattern occurred earlier than for uniform heat flux.

Chen et al. [31] investigated the heat transfer coefficient of saturated liquid R-134a on the verge of commencing flow boiling under flow rate oscillations. They conducted tests in a narrow annular duct with a hydraulic diameter of 4 mm under a mean mass flux of 300 to 500 kg/m²s. Saturation temperatures were varied between 10 and 15 °C, with a heat flux of 0 to 45 kW/m². The oscillations were of a triangular form, with an amplitude varying between 0% and 30% of the mass flux under investigation. The period of the oscillation ranged between 20 and 120 s. It was found that the time-averaged heat transfer coefficients were not noticeably affected by either the amplitude or the period of the mass flux oscillation.

Studies that directly consider the effect of an unsteady heat flux are limited. Chen et al. [32] investigated the effect of an oscillating heat flux on the heat transfer of R-134a in an annular duct. The duct consisted of an outer Pyrex glass pipe with an inner diameter of 20 mm in which the refrigerant flowed. Inside this was a smooth copper pipe with an outer diameter of 10, 16, or 18 mm, corresponding to hydraulic diameters of 10, 4 and 2 mm. The inner pipe wall thicknesses were 1, 1.5, and 2.5 mm respectively. The heat flux was provided by a cartridge heater inside this copper pipe. A saturated liquid inlet state at 15 °C was used and constant mass fluxes of 300 and 500 kg/m²s were considered. The heat flux in the inner pipe was oscillated in a triangular wave between 0 and 30 kW/m² with a mean heat flux of 15 kW/m², over periods

by molten salt technologies. This can ultimately result in improved thermodynamic energy conversion efficiencies, and lower capital and operating costs.

Depending on the heat flux densities and operating temperature requirements, organic working fluids can also be considered instead of water [13, 14]. This results in the term “organic Rankine cycles (ORCs)”, and is of particular interest in distributed, low-concentration [5] or dual-fuel [15] systems. The lower associated operating pressure, also makes this an attractive option for DSG CSP. Many different fluids, including alkanes, ammonia and refrigerants such as R-134a and R-245fa (amongst others) have been considered for different applications [16–18]. Specifically, theoretical studies of such solar ORC systems have suggested system effi-

of 2 to 600 s. It was found that the influence on the time-averaged heat transfer coefficient was negligible, regardless of the amplitude or period of the heat flux oscillation. The wall temperature of the inner pipe followed the imposed heat flux, with a time lag due to the thermal inertia of the copper wall. When the period of oscillation was small enough (2 s), the wall temperature was unaffected.

Park et al. [33] conducted a study on the possible detrimental effect of repeated flow oscillations on the heat transfer coefficient of R-134a at a mean mass flux of 300 kg/m²s. They used a stainless-steel pipe with a 5 mm bore, at a saturation temperature of 27 °C. The heat flux was kept between 10.3 and 11.2 kW/m². The flow was oscillated sinusoidally with an amplitude of 59% to 131% of the mean mass flux, for periods between 10 and 130 s. It was found that, if the amplitude and period of oscillation remained below a certain threshold, the mean heat transfer coefficient remained unaffected. The wall temperature closely followed the oscillation for certain periods and amplitudes.

Wang et al. [34] conducted a study of the influence of an imposed heat flux oscillation on the onset of boiling and the heat transfer coefficient of saturated liquid FC-72 flowing over a flat plate. They considered a rectangular waveform with an amplitude of 10 to 50% of the mean heat flux (10 kW/m²) and periods of between 10 and 30 s, at a saturation temperature of 55 °C. The time-averaged heat transfer coefficient was found to be unaffected by the imposed waveform, but the instantaneous temperature measured at the wall followed the imposed heat flux with a delay.

The fact that the measured wall temperature fluctuates with the applied heat flux as reported in the literature investigating transient heat fluxes opens up another possible failure mechanism particular to CSP systems. In an industrial parabolic trough system, the receiver geometry consists of a metal tube inside a glass sheath, responsible for maintaining a vacuum around the tube in order to limit heat transfer losses. This seal can be broken for many reasons, which make the replacement of these evacuated tubes one of the chief operating costs encountered in practice [35]. Although it is not the subject of this particular study, it is interesting to note that many studies have been conducted in an attempt to quantify and solve this problem [36–41]. Any temperature response data gathered is thus also of interest to engineers developing parabolic trough systems.

To the authors' knowledge, there has been a scarcity of experimental research focused on actual DNI data, and in particular on any temporal fluctuations to the imposed heat flux due to transient variations in the DNI. The effect of these conditions on the heat transfer and pressure drop in boiling flows through horizontal pipes has yet to be studied in detail.

In a previous paper [42], the influence of an inlet vapour quality perturbation on the heat transfer coefficient was considered. It was found that the expected heat transfer coefficient differed by up to 30% from the achieved value, and that there was an under- and overprediction during the downward and upward perturbations. While the heat transfer coefficient is nominally independent of the heat flux, many studies on two-phase boiling flow in particular have found that this is not the case. The steady-state heat transfer coefficient depends on the applied heat flux in many instances.

In this study, perturbations of the heat flux during saturated flow boiling are considered, with particular focus on the instantaneous heat transfer coefficient, wall temperature and pressure drop in a horizontal pipe. R-245fa is selected as fluid because of its benign nature, low saturation pressure, and the fact that it is being actively investigated for use in many practical applications [43–45]. Additionally, guidelines for the development of experimental facilities with which to conduct these tests are in their infancy, which this study also aims to address.

2. Experimental methods

2.1. Facility and apparatus

The experimental set-up, which consisted of a closed refrigerant loop operated with R-245fa, is shown schematically in Fig. 1. It has been reported in a previous article [42], but for the benefit of the reader, the relevant aspects are briefly repeated here. Subcooled liquid was pumped from the liquid receiver and circulated through the electrically heated preheater (between Points A and B), the electrically heated test section (between Points C and D), and a water-cooled condenser (between Points E and F). The preheater was used to control the inlet vapour quality to the test section, while the test section was used to perform diabatic thermal measurements from which to derive the flow boiling heat transfer coefficients. The condenser was used to remove the heat added to the fluid in the preheater and test section, and to return the fluid to a subcooled liquid state. By altering the condenser water flow rate, the overall operating pressure and the associated saturation temperature could be adjusted.

The entire facility, except the test section, was constructed from smooth hard-drawn copper pipe with an outer diameter of 12.7 mm. To ensure that only liquid entered the pump, the liquid receiver (which had a capacity of 18 L) was placed approximately 1.5 m above the pump suction side. A GATHER magnetically coupled variable speed gear pump (with a rated operating range of 14.4 to 540 L/h) was used to control the mass flow rate through the test section. When required, small adjustments to the flow rate could also be made via a bypass line equipped with a hand-operated needle valve. The test line mass flow rate was measured with a MicroMotion CMF010 Coriolis flow meter which had a maximum rated range of 0.04 kg/s with an accuracy of 0.1% of the flow rate.

The preheater consisted of two 1.9 m copper pipe sections onto which electrically insulated constantan wire was wound tightly around the circumference. Each section had a resulting electrical resistance of 35 Ω and was connected separately to two 3 kW ElektroAutomatik EA8360-30 DC power supply units which had an accuracy of 0.2% of the output voltage and current. The test section, which consisted of two sight-glasses, a heated copper tube, and several temperature and pressure measurement probes are discussed in detail in the next section. The condenser (a tube-in-tube heat exchanger) was connected to a large external water reservoir which provided cooling water at approximately 6 °C. The water was circulated via a fixed-speed EBARA centrifugal pump and the water flow rate was adjusted with a three-way valve. A MicroMotion CMF025 Coriolis flow with a maximum flow rate of 0.4 kg/s, and an accuracy of 0.1% of the current flow rate was used to measure this water flow rate.

For monitoring and control purposes, several pressure transducers, thermocouples and resistance temperature detectors (RTDs) were installed at the locations indicated in Fig. 1 by **P**, **T**, and **RTD** respectively. GEMS 2200 series absolute pressure transducers, with an accuracy of 0.2% of the full scale (which was 2 MPa) were used before and after the gear pump. All other pressure monitoring locations were equipped with Sensotec FP2000 absolute pressure transducers, with an accuracy of 0.25% of the full scale of 3.4 MPa. All pressure taps were orientated horizontally and had a diameter of 0.8 mm, which was smaller than 10% of the pipe diameter. Thermocouple measuring locations (**T**) were each equipped with four T-type thermocouples (with an 0.1 °C accuracy each before calibration) positioned externally around the pipe circumference on the top, bottom, left, and right, and attached with thermal tape. Additional temperature measurement was done via Omega 1/10 DIN Pt100 RTDs (0.03 °C accurate) directly before the preheater, directly before the test section, directly after the test section, and directly after the condenser. Thermal insulation with a conductiv-

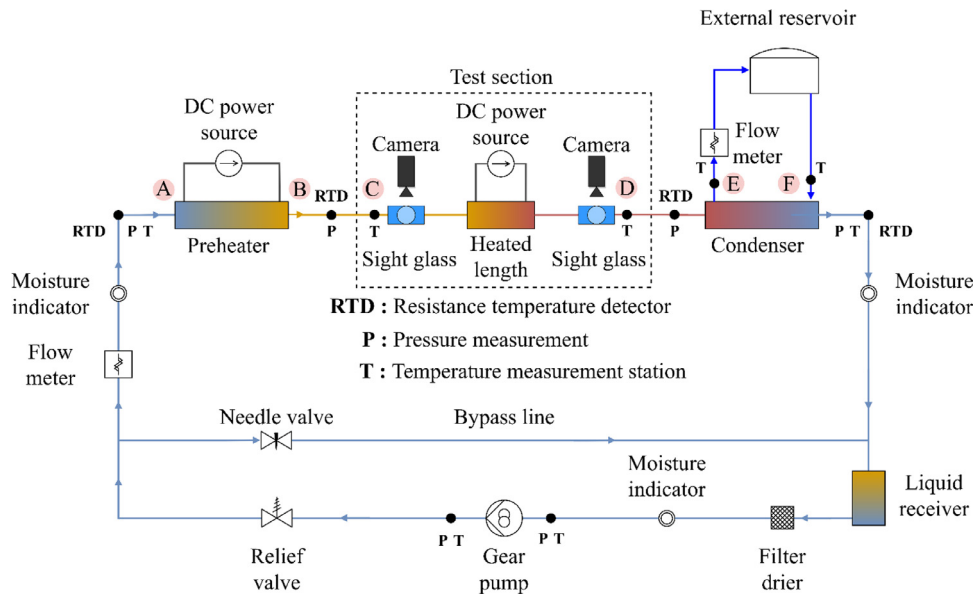
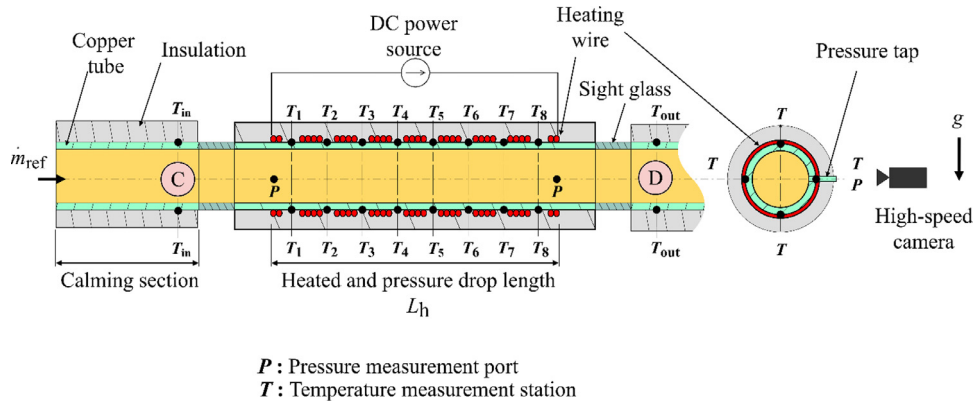


Fig. 1. Experimental test facility schematic showing flow boiling apparatus.



P : Pressure measurement port
T : Temperature measurement station

Fig. 2. Test section schematic (not to scale).

ity of 0.036 W/mK [46] was installed to a minimum radius of 80 mm around the entire flow loop.

2.2. Test section

Because linear focal methods in CSP uses collector tubes that are installed in a near-horizontal inclination, a horizontal test section arrangement was considered in this study. The test section, shown in Fig. 2, consisted of a calming section with a length of 500 mm, an inlet sight glass, a heated length (L_h) of 800 mm, and an outlet sight glass. The calming and heated section were constructed from hard-drawn copper pipe with an outer diameter (d_o) of 9.53 mm and an inner diameter (d_i) of 8.31 mm. In order to compare results with existing studies in the literature, the inner diameter was selected such that the pipe was in the conventional size range (larger than 3 mm inner diameter [47]).

In order to reduce interference of upstream bends, the length of the calming section was selected to be approximately 60 times the internal diameter. This satisfies the recommendations of Cho and Tae [48] who found that upstream flow disturbances caused by bends and twists can influence the downstream flow characteristic and heat transfer mechanism for a length of up to 48 times the internal diameter. To retain a smooth transition before and after the heated length, the sight glasses had the same inner diameter

as that of the copper pipe. Both the inlet and outlet sight glasses were manufactured from 60 mm long borosilicate glass tubes, with a thermal conductivity of 1.14 W/mK.

A heating method similar to that used in the preheater was used in the test section. An electrically insulated constantan resistance wire (coloured red in Fig. 2) with a resistance of 180 Ω was wound tightly around the tube over a length of L_h (800 mm). It was connected to an adjustable 1.5 kW ElektroAutomatik EA8360-15 DC power supply with an accuracy of 0.2% of the output voltage and current.

Several thermocouple locations (black circles and labelled T in Fig. 2) were used. The inlet and outlet fluid temperatures (T_{in} and T_{out}) were measured before and after the inlet and outlet sight glasses by four T-type thermocouples each, spaced equally around the circumference of the tube (top, bottom, left and right). The tips were located in shallow divots and then soldered in position. The wall temperature profile along the length and around the circumference of the heated portion was determined via 32 T-type thermocouples that were installed in a similar way. The thermocouples were grouped in 8 sets of 4 thermocouples each (spaced equally along the axial length at a pitch of 100 mm and also located at the top, bottom, left and right). Care was taken to prevent direct heating of the thermocouple tips from the neighbouring heating element passes by leaving gaps around the tips.

Table 1
Selected thermophysical properties of R-245fa at a saturation temperature of 35°C [49].

Pressure (kPa)	Density (kg/m ³)		Specific enthalpy (kJ/kg)		Specific heat (kJ/kgK)	
	Liquid	Vapour	Liquid	Vapour	Liquid	Vapour
212	1311	12	246	432	1.34	0.935

The inlet and outlet absolute pressure over the test section were measured by Sensotec FP2000 transducers (as mentioned previously). The differential pressure was measured using a Validyne DP15 transducer. The differential pressure transducer had an 8.6 kPa membrane installed and had an accuracy of 0.5% of this full scale. The inlet and outlet pressure taps were located as indicated by **P** in Fig. 2, 800 mm (L_h) apart, and had the same relative size as the other pressure taps mentioned previously.

The test section was insulated to a minimum radius of 100 mm using the same type of insulation mentioned previously. Calculations were done under worst-case scenarios that showed that the heat loss from the test section was less than 0.5% of the applied heat in this study.

A specialised Photron Mini-UX high-speed camera was used at the inlet and outlet sight glass during this study to record and verify the flow patterns. It had a maximum resolution of 1 280 by 1 024 pixels, a maximum frame rate of 4 000 frames per second, and an internal memory capacity of 8 GB.

2.3. Experimental procedure

2.3.1. Calibration

Because the accuracy of test section temperature measurement was of significant importance, special care was taken to calibrate the thermocouples indicated in Fig. 2. For this purpose, two pre-calibrated Pt100 resistance temperature detectors (with an accuracy of 0.03 °C) were mounted ahead and after the test section (ahead of Point C and after Point D in Fig. 1 and Fig. 2), such that their measuring tips were wholly immersed in the fluid flow. The wall thermocouples were calibrated *in situ* against these Pt100s during adiabatic and isothermal steady-state conditions by passing a single-phase liquid at the desired temperature through the test section. This procedure was repeated at intervals of 5 °C between 15 °C and 45 °C, and the obtained data was used to derive calibration curves for each thermocouple. Following calibration, the thermocouples had an average accuracy of 0.05 °C, less than the manufacturer's stated accuracy of 0.1 °C. In the interests of conservatism, the manufacturer's value was used.

The differential pressure transducer was calibrated to an accuracy of 0.2% by using a digital manometer with an accuracy of 0.5% of the full scale with a water-filled U-tube manometer.

2.3.2. Test matrix and measurement procedure

A mass flux (G) of 200 kg/m²s was considered because the resulting flows observed in the pipe diameter fell within the range of regimes encountered in applications of interest (in particular DSG). A saturation temperature of 35°C was chosen chiefly because of safety concerns. Although lower than the minimum found in the boiling sections of actual low-temperature ORC systems (which are upwards of 80°C), it still falls within the temperature range for electronics cooling, battery cooling systems, and waste heat recovery applications. Some thermophysical properties for R-245fa at 35°C are shown in Table 1.

The reference heat flux (before and after the perturbation) was selected to be 7.5 kW/m² (which is easily achievable in small parabolic troughs [10]) and was based on the expected operation of a small solar-driven ORC system at a DNI of 0.75 kW/m² and a concentration ratio of 10. In order to determine the amplitude,

period, and perturbation time profile of interest during conditions of temporary cloud coverage, actual weather data was considered. For this purpose, DNI data (measured by a Kipp and Zonen CHP1 pyrhelimeter, with a maximum uncertainty of 2% of the current reading, and logged at intervals of 60 s) was obtained from a weather station located at the University of Pretoria in South Africa (25.7545° S, 28.2314° E, elevation 1 339 m). Even though the rate of the decrease in DNI depended on aspects such as cloud density and wind speeds, some insights were obtained from the weather station data. A typical cloudy and windy day on 26 August 2017 was selected at random. The recorded DNI data from 06:00 in the morning to 18:00 in the evening is presented in Fig. 3a. A detailed 30-min window during mid-morning between 10:30 am and 11:00 am, is shown in Fig. 3b, along with the measurement accuracy of each data point.

Fig. 3b indicates that the DNI varied significantly from a high of approximately 0.8 kW/m² at 10:32 to a low of 0.2 kW/m² at 10:33, which represented a DNI reduction of 75%. The recorded wind speed was approximately 20 km/h. Coupled with the cloud cover, this scatter is understandable. Unfortunately, the temporal resolution of the recording instrumentation was not high enough to capture the actual DNI on a sub-minute scale, but based on the minute scale data, it is clear that within a one-minute time interval, large perturbations in the DNI were present.

In order to represent a hypothetical set of sub-minute scale behaviours, three DNI perturbation time profile types were considered in this research. These are indicated in Fig. 4, and include a step pulse (indicated in blue), a triangular ramp-down and ramp-up pulse (indicated in pink) and a sinusoidal reduction and recovery pulse (indicated in teal). In all of these profiles, a temporal reduction of 75% of the concentrated DNI was considered, and was based on the measured DNI reductions mentioned previously. A time length of 30 s was selected because it reflected the timescale of the drastic changes presented in Fig. 3b. The three shapes of the perturbations were chosen to vary between extremely rapid cloud coverage (the step perturbation) and a more moderate, constant rate of cloud coverage (the triangular perturbation). The sinusoid was chosen to represent winds driving clouds that can affect the incident sunlight. These shapes also corresponded to the observed shapes in Fig. 3b. The indicated numbers (1 to 4) in Fig. 4 signify the time instance points at the start, middle and end of the perturbation pulses, as well as a restored steady state after the perturbation. These instances are referred to in the results discussion section.

As mentioned earlier, the inlet thermodynamic state to the test section was primarily selected to cover some commonly expected flow patterns. Fig. 5 shows a Wojtan-Ursenbacher-Thome [50] flow pattern map constructed based on the selected mass flux, heat flux and saturation temperature. Tests were conducted at 16 different inlet vapour quality conditions (x_{in}) ranging from 0.1 to 0.85 at intervals of 0.05. The figure indicates that the majority of test conditions were anticipated to fall within the annular flow pattern region, with the rest being slug or intermittent flow. The prevalence of these flow patterns was visually confirmed via the high-speed camera, as shown later in Fig. 6.

It is important to note that even though the inlet vapour quality was held constant during each experiment, the variation of the applied heat flux had an influence on the average vapour quality in

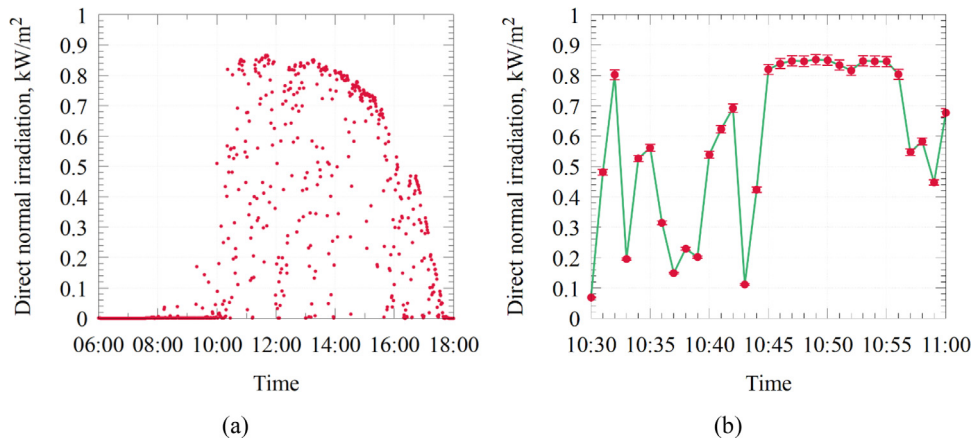


Fig. 3. Direct normal irradiation (DNI) measured on 26 August 2017 for: (a) all sunlit daytime hours, and (b) a 30-min view from 10:30 am to 11:00 am.

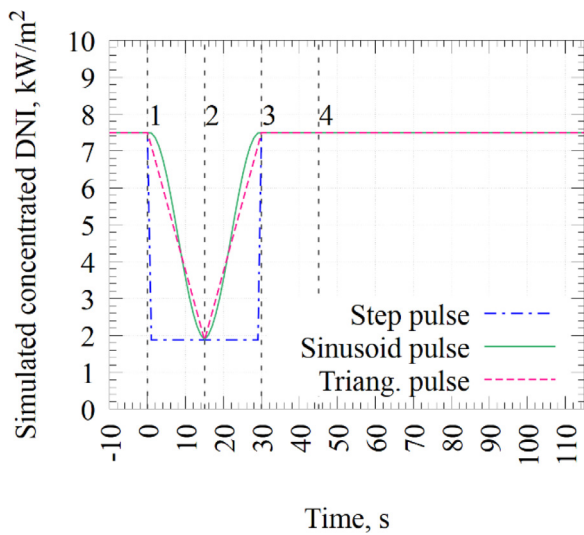


Fig. 4. Applied perturbation time profiles under consideration.

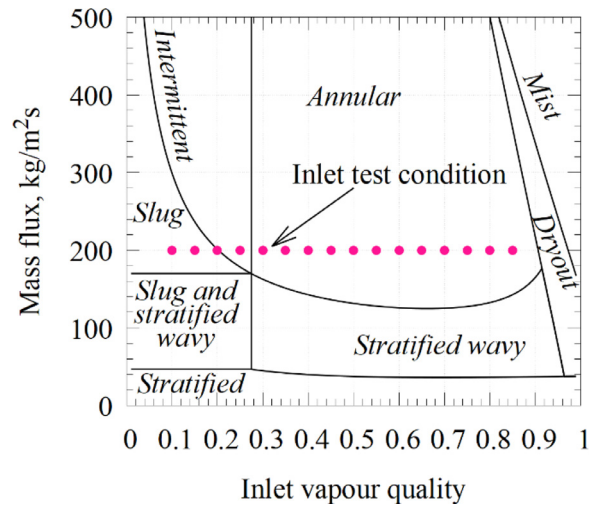


Fig. 5. Inlet test conditions plotted on a Wojtan-Ursenbacher-Thome [50] flow pattern map, constructed specifically for a mass flux of $200 \text{ kg/m}^2\text{s}$, heat flux of 7.5 kW/m^2 , and saturation temperature of 35°C .

the test section, and is discussed in more detail later. At steady-state conditions, the vapour quality increased by approximately 0.08 from the inlet to the outlet of the heated length. All inlet conditions were investigated for each of the previously-mentioned

perturbation cases (Fig. 4), while the behaviour under steady-state conditions was used as the reference datum condition.

In order to confirm the presence of the flow patterns indicated in Fig. 5, the high-speed camera in Fig. 2 was utilised. Recordings

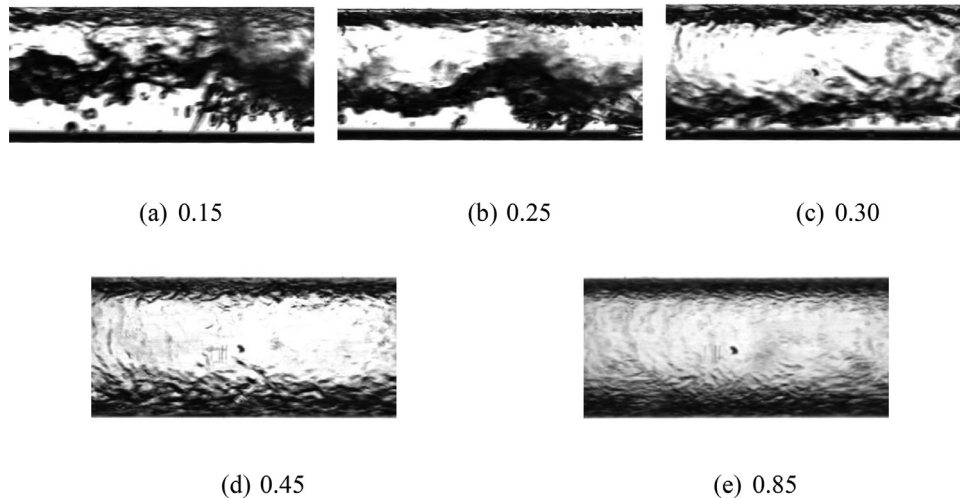


Fig. 6. Flow patterns observed at an inlet vapour quality of (a) 0.15, (b) 0.25, (c) 0.30, (d) 0.45, and (e) 0.85.

of all the vapour qualities in the test matrix were captured at 2 000 frames per second at a resolution of 1 280 by 720 pixels at the inlet sight glass. Screenshots of the recordings for specific vapour qualities of interest are shown in Fig. 6. The vapour qualities of 0.15 (Fig. 6a), 0.25 (Fig. 6b), and 0.30 (Fig. 6c) were chosen since they straddle the transition lines in Fig. 5 at a mass flux of 200 kg/m²s, while the vapour qualities of 0.45 and 0.85 (Figs. 6d and 6e) were used to confirm annular behaviour.

According to Fig. 5, a vapour quality of 0.15 should show a slug flow pattern. The observed flow pattern alternated between intermittent and slug flow however, which should only happen at a vapour quality of 0.20. This indicates that the flow pattern map transition between slug and intermittent flow possibly needs adjustment. A vapour quality of 0.25 showed the intermittent flow pattern, agreeing with the flow pattern map. The annular flow pattern was visible for vapour qualities 0.3 and up, confirming the accuracy of the flow pattern map. The flow patterns for the majority of vapour qualities tested (0.30 to 0.85) were thus of the form most often encountered in industrial systems (that of annular) and the flow pattern map was deemed sufficiently accurate.

All perturbations and the data logging procedure were initiated once steady state conditions had been achieved for at least 20 min. This was judged to have been reached when the mass flux remained within 2.5% of 200 kg/m²s, the saturation temperature was within 0.5 °C of 35 °C and the actual inlet vapour quality was within 0.03 of the target vapour quality. The upper and lower limiting values for the flow to be considered steady state were explicitly chosen to fall outside the uncertainty band. Once steady state had been achieved, and the overall test facility energy balance error percentage (calculated below in Eq. (1)) was < 5%, a perturbation was initiated, as a single-pulse profile (step, triangular or sinusoidal). Data samples were captured at approximately 2 Hz to match the ability of the power supply control interfaces.

2.3.3. Data processing and analysis

A key metric in achieving a steady state operating condition is the diabatic energy balance error. This entails accounting for all the energy added or removed in the control volume consisting of the preheater, test section and condenser:

$$\%EB = 100 \left(1 - \frac{\dot{Q}_{pre} + \dot{Q}_{test}}{\dot{Q}_{cond}} \right) \quad (1)$$

where \dot{Q}_{pre} is the heating rate in the preheater, \dot{Q}_{test} is the heating rate in the test section, and \dot{Q}_{cond} is the heat transfer rate removed in the condenser. The pumping power to the gear pump and heat loss or gain from the test facility tubing through the insulation were ignored because the losses through the insulation was less than 0.5% (as described previously) and the pump was not part of the control volume under investigation.

The condensation heat transfer rate was determined via the energy balance principle based on the water-side measurements:

$$\dot{Q}_{cond} = \dot{m}_w (h_{w,out} - h_{w,in}) \quad (2)$$

where \dot{m}_w is the mass flow rate of the water obtained from the water Coriolis flow meter, and $h_{w,out}$ and $h_{w,in}$ are the specific enthalpies of the water at the outlet and inlet. These were obtained from the measured water temperature at Points E and F in Fig. 1 via the CoolProp thermodynamic library [49].

The heating rate of the preheater was determined using the generalised power equation, neglecting heat loss through the preheater thermal insulation:

$$\dot{Q}_{pre} = V_{pre} I_{pre} \quad (3)$$

where V_{pre} and I_{pre} are the voltage and current of the preheater power supply unit, as obtained from the instantaneous values communicated to the control software. The heating rate of the test sec-

tion was determined in a similar way, but based on the voltage and current applied to the test section.

Next, the inlet vapour quality of the R-245fa was verified by using the following definition:

$$x_{in} = \frac{h_{in} - h_f}{h_g - h_f} \quad (4)$$

where h_{in} is the inlet specific enthalpy, and h_f and h_g are the specific enthalpies of the saturated liquid and vapour, respectively. The latter enthalpies were obtained from CoolProp [49] at the governing saturation temperature, calculated as the arithmetic averaged temperature in the test section based on the inlet and outlet R-245fa temperatures (as discussed later). h_{in} was calculated from the energy balance around the preheater located between Points A and B (see Fig. 1), and the adiabatic fluid line between Points B and C:

$$h_{in} = h_C = h_B = \frac{\dot{Q}_{pre}}{\dot{m}_{ref}} + h_A \quad (5)$$

Here \dot{m}_{ref} is the mass flow rate of the R-245fa obtained from the refrigerant line Coriolis flow meter, and h_A , h_B , and h_C are the specific enthalpies of the fluid at Points A, B, and C. The value of h_A was obtained from the measured temperature and pressure at Point A via CoolProp [49].

The instantaneous heat transfer coefficient at time t , $\alpha(t)$, was determined using Newton's law of cooling as is common in engineering practice:

$$\alpha(t) = \frac{\dot{q}_i(t)}{\bar{T}_{i,wall}(t) - T_{sat}} \quad (6)$$

with $\dot{q}_i(t)$ being the instantaneous inner-surface (wall) heat flux, T_{sat} being the saturation temperature over the test section, and $\bar{T}_{i,wall}(t) \approx \bar{T}_{wall}(t)$ being the instantaneous spatially-averaged wall temperature determined from the 32 wall thermocouples. The assumption that the inner and outer wall temperature were equivalent, was checked against a lumped capacitance analysis and Fourier conduction calculation as mentioned later.

The saturation temperatures before and after the heated section were obtained from the arithmetic averages of the thermocouple measurements at stations T_{in} and T_{out} . These were compared against the readings obtained from the two Pt100s before and after the test section and also cross-checked against the expected saturation temperature at the recorded absolute pressure readings from the locations indicated in Fig. 2. It was found for adiabatic conditions that the Pt100 readings and the thermocouple readings were within 0.1 °C of each other.

The inner-surface heat flux was calculated from an unsteady energy equation, as follows:

$$\dot{q}_i(t) = \dot{q}_{test}(t) - \dot{q}_{Cu}(t); \quad \dot{q}_{Cu}(t) = \frac{\dot{Q}_{Cu}}{A_s}; \quad \dot{q}_{test}(t) = \frac{\dot{Q}_{test}(t)}{A_s} \quad (7)$$

where $A_s = \pi d_i L_h$ is the inner-wall surface area based on the inner pipe diameter and the heated length, while $\dot{q}_i(t)$ is the net heat flux on the inner wall (imposed from the solid wall onto the flow of R-245fa) at time t . The latter was calculated from the known applied electric heating power (\dot{Q}_{test}) and the unsteady heat accumulation in the copper pipe wall (\dot{Q}_{Cu}). This energy balance assumes that the heat transfer through the exterior thermal insulation is negligible. Also note that under steady-state conditions, $\dot{Q}_{Cu} = \dot{q}_{Cu} = 0$.

As before, $\dot{Q}_{test}(t)$ was determined using the instantaneous voltage (V_{test}) and current (I_{test}) readings from the power supply control interface, while the heat accumulation in the copper was obtained by calculating the change in energy content of the pipe wall over a certain time:

$$\dot{Q}_{Cu}(t) = m_{Cu} c_p \frac{dT_{wall}(t)}{dt} \quad (8)$$

Here, m_{Cu} is the mass of the pipe, determined from the density and volume of copper, and c_p is the specific heat capacity of the pipe wall material (obtained from Ref. [51]).

To check the assumption that the wall temperature was radially approximately uniform, the Biot number was calculated as follows:

$$Bi = \frac{\alpha L_C}{k_{wall}} \quad (9)$$

where α is the heat transfer coefficient, k_{wall} is the wall thermal conductivity, and L_C is the characteristic length, defined in terms of the copper volume (V_{Cu}) and the inner surface area (A_s) as:

$$L_C = \frac{V_{Cu}}{A_s} = \frac{\frac{\pi}{4}(d_o^2 - d_i^2)L_h}{\pi d_i L_h} = \frac{d_o^2 - d_i^2}{4d_i} \quad (10)$$

It was found that for a sampling interval of $\Delta t \approx 0.5$ s, the Biot number was an order of magnitude smaller than 0.1 in the worst case considered. This indicates that there was an undetectable instantaneous difference between the outer-wall (measured), inner-wall and average wall temperatures. This was also confirmed via a one-dimensional Fourier conduction calculation based on the thermal resistance of the copper wall. The difference in temperature between the outer and inner wall was found to be less than 0.01°C , and thus could be considered negligible.

The total pressure difference (Δp_{total}) was obtained from the differential pressure transducer. This difference can be separated into the contributions of the static pressure difference (Δp_{static}), the momentum pressure difference (Δp_{mom}), and the frictional pressure drop (Δp_{frict}) as:

$$\Delta p_{total} = \Delta p_{static} + \Delta p_{mom} + \Delta p_{frict} \quad (11)$$

Because the test section was horizontal, the static pressure difference (elevation head) was disregarded. Since the heated length, L_h , was also the length between the pressure ports on the test section, the frictional pressure drop gradient was calculated as follows:

$$\frac{\Delta p_{frict}}{L_h} = \frac{\Delta p_{total} - \Delta p_{mom}}{L_h} \quad (12)$$

The momentum pressure drop was calculated using the following equation [52]:

$$\Delta p_{mom} = G^2 \left\{ \left[\frac{(1 - x_{out})^2}{\rho_f(1 - \varepsilon_{out})} + \frac{x_{out}^2}{\rho_g \varepsilon_{out}} \right] - \left[\frac{(1 - x_{in})^2}{\rho_f(1 - \varepsilon_{in})} + \frac{x_{in}^2}{\rho_g \varepsilon_{in}} \right] \right\} \quad (13)$$

in which G is the mass flux of the refrigerant through the test section, ρ_f and ρ_g are the densities of the saturated liquid and vapour respectively, and ε_{out} and ε_{in} refer to the void fraction at the outlet and inlet to the test section. The void fraction was calculated using the Steiner [53] adaptation for horizontal tubes of the Rouhani-Axelsson [54] drift flux model:

$$\varepsilon = \frac{x}{\rho_g} \left\{ \left[1 + 0.12(1 - x) \right] \left(\frac{x}{\rho_g} + \frac{1 - x}{\rho_f} \right) + \frac{1.18}{G} \left[\frac{g\sigma(\rho_f - \rho_g)}{\rho_f^2} \right]^{0.25} (1 - x) \right\}^{-1} \quad (14)$$

in which σ refers to the surface tension of the fluid and x refers to the relevant local vapour quality (inlet or outlet).

2.3.4. Uncertainty analysis

The uncertainties of the calculated and measured values were determined using the method proposed by Dunn and Davis [55], and are shown in Table 2.

Table 2
Parameter ranges and uncertainties.

Parameter	Range	Uncertainty
Singular temperature measurement point	35 – 45°C	0.1°C
Mass flux (G)	200 kg/m ² s	0.6%
Inlet vapour quality (x_{in})	0.10 – 0.85	0.03
Heat flux (\dot{q})	1.9 – 7.5 kW/m ²	0.4%
Heat transfer coefficient (α)	1.5 – 7.0 kW/m ² K	2%
Differential pressure (dP)	-8.6 – 8.6 kPa	0.043

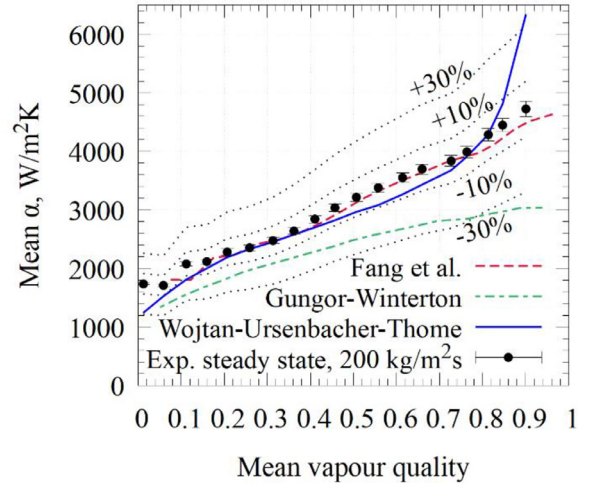


Fig. 7. Two-phase flow validation, showing steady-state mean heat transfer coefficients for a mass flux of 200 kg/m²s, heat flux of 7.5 kW/m², and saturation temperature of 35°C with predicted values.

2.3.5. Validation

Before the main testing commenced, several validations were done covering both single- and two-phase flow conditions for quality assurance purposes. Single-phase liquid validation consisted of determining experimental Nusselt numbers for various Reynolds numbers and comparing them against those predicted by existing correlations. It was found that the system delivered Nusselt numbers within 5% of those predicted by the Gnielinski [56] and Meyer et al. [57] correlations. Full details can be found in previous work [42].

The two-phase boiling validation was done by obtaining the steady-state heat transfer coefficients for the entire vapour quality range at a mass flux of 200 kg/m²s, a heat flux of 7.5 kW/m², and a saturation temperature of 35 °C. Experimentally-derived values were compared against predictions by the Wojtan-Ursenbacher-Thome [58], Fang et al. [59] and Gungor-Winterton [60] correlations, as indicated in Fig. 7. For reference, $\pm 10\%$ and $\pm 30\%$ bands above and below the experimentally obtained heat transfer coefficient are also included as black dotted lines.

It was found that the experimentally-derived heat transfer coefficients were within 10% of the Fang et al. [59] and Wojtan-Ursenbacher-Thome [58] correlation predictions and within 30% of the Gungor-Winterton [60] correlation prediction for almost all vapour quality conditions.

3. Results and discussion

Consider Fig. 8 for an inlet vapour quality of 0.30. The response for all three perturbation types (step, sinusoidal and triangular) is included and indicated by the blue, teal and pink lines, respectively. The instantaneous inner-wall heat flux (Eq. (7)) is plotted in Fig. 8a, while the response of the measured wall and saturation temperatures is given in Fig. 8b. The spatially-averaged heat transfer coefficients are shown in Fig. 8c. The mean heat transfer co-

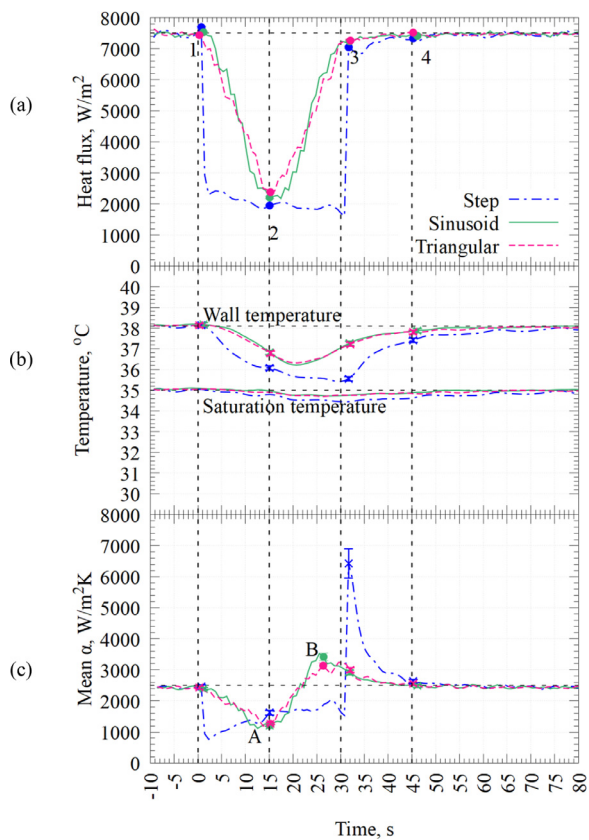


Fig. 8. (a) Step, sinusoidal and triangular heat flux perturbations, and response of (b) wall and saturation temperatures, and (c) mean heat transfer coefficient for a vapour quality of 0.30, mass flux of 200 kg/m²s, and initial heat flux of 7.5 kW/m².

efficient shown is the instantaneous value obtained using Eq. (6), in which the mean of the eight thermocouple stations (T_1 to T_8 in Fig. 2) is used. The timescale covered is 90 s, starting 10 s before the introduction of the perturbation, including the 30 s span of the perturbation, and running until 50 s after the perturbation was completed. The cause for the jagged appearance of the heat flux was the sampling rate at which the power supply interfaces responded to commands from the controlling software.

For ease of discussion, the four instance points indicated in Fig. 4 are also highlighted in Fig. 8. As mentioned, these points represent the moments immediately before the perturbation at time 0 s (1), midway through the perturbation at time 15 s (2), the end of the perturbation at time 30 s (3), and long after the perturbation pulse to represent a return to steady state at time 45 s (4). The uncertainties for the temperatures and heat transfer coefficient are also shown at these points for illustrative purposes.

During the step perturbation (the blue line in Fig. 8), the discharge from the copper pipe is most visible, as can be judged by the steady downward gradient in the instantaneous inner-surface heat flux between Points 1 and 3. During this time, the copper discharged approximately 70% of its available thermal energy to the fluid. The rate at which this discharge occurred decreased as the wall temperature approached the R-245fa saturation temperature. The initiation of the single-step perturbation at Point 1 (at time reference 0 s) almost immediately had an effect on the heat transfer coefficient. The coefficient dropped from the initial steady-state value of approximately 2 400 W/m²K to a value of approximately 800 W/m²K (33% of its initial value), and recovered to a pseudo-steady-state value of approximately 1 900 W/m²K (80% of its initial value) in the first 25 s of the perturbation, before the upward step occurred. Almost immediately after the upward step occurred, the

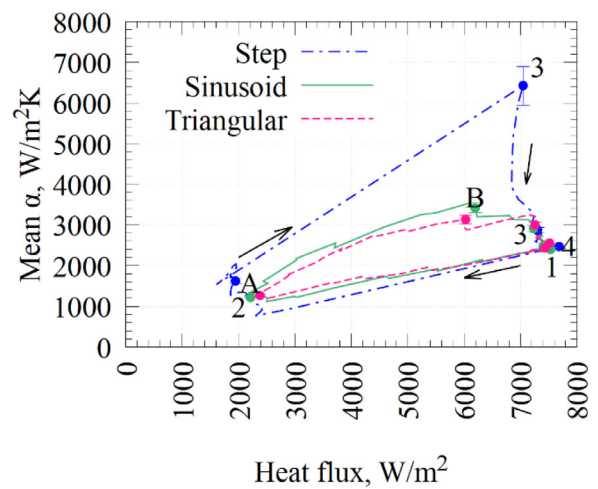


Fig. 9. Heat transfer coefficient as a function of the actual heat flux for step, sinusoidal and triangular heat flux waveforms for a vapour quality of 0.30, mass flux of 200 kg/m²s, and initial heat flux of 7.5 kW/m².

heat transfer coefficient spiked to a value of approximately 6 400 W/m²K (166% higher than the initial value) before settling back to its pre-perturbation value of 2 400 W/m²K at Point 4. It is important to note that the heat transfer coefficient did not mirror the applied heat flux during the time span of the heat flux perturbation. This is clear from the mentioned relative percentage increases or decreases in the heat transfer coefficient, which do not align with the relative reduction and increase in the inner-wall heat flux. Of interest to note is that due to the thermal wall storage effect, the heat flux did not immediately return to its unperturbed level of 7.5 kW/m² at Point 3, but rather took approximately ten seconds to do so.

Next, the sinusoidal and triangular perturbations (teal and pink lines in Fig. 8) are considered. Based on the actual inner-wall heat flux profiles, these two perturbations are almost indistinguishable, meaning the resulting temperature measurements and calculated heat transfer coefficient will largely be the same. Therefore, the general trends of both perturbation types are discussed together. Also included in Fig. 8 are Points A and B, which denote the time during these perturbations when the heat transfer coefficient exhibited a local minimum and maximum respectively. For the example case presented in Fig. 8 with an inlet vapour quality of 0.3, the minimum and maximum heat transfer coefficient occurred at approximately 14 s and 26 s after the initiation of the perturbation. While Point A almost coincided with Point 2 (when the applied heat flux was at its lowest), Point B occurred before the maximum heat flux was at its highest (i.e., before Point 3).

Once again, the heat transfer coefficient did not mirror the applied heat flux. The heat transfer coefficient reached a local minimum of approximately 1 200 W/m²K (50% of the initial value) at Point A, even though the inner-wall heat flux was at its minimum at that point (75% lower than the unperturbed value). However, at Point B, the heat transfer coefficient reached a maximum of 3 400 W/m²K (42% higher than its initial value), while the inner-wall heat flux was still recovering and was at 80% of its initial value. Once the perturbation was complete, the heat transfer coefficient again returned to the unperturbed level at Point 4.

Fig. 9 offers a different perspective on the obtained results and can be used to better visualise the influence of the heat flux on the heat transfer coefficient. The instantaneous heat transfer coefficient is plotted against the instantaneous inner-wall heat flux for each of the perturbation profiles. For reference, the same time instance points (1 to 4) as well as Points A and B in Fig. 8c are also

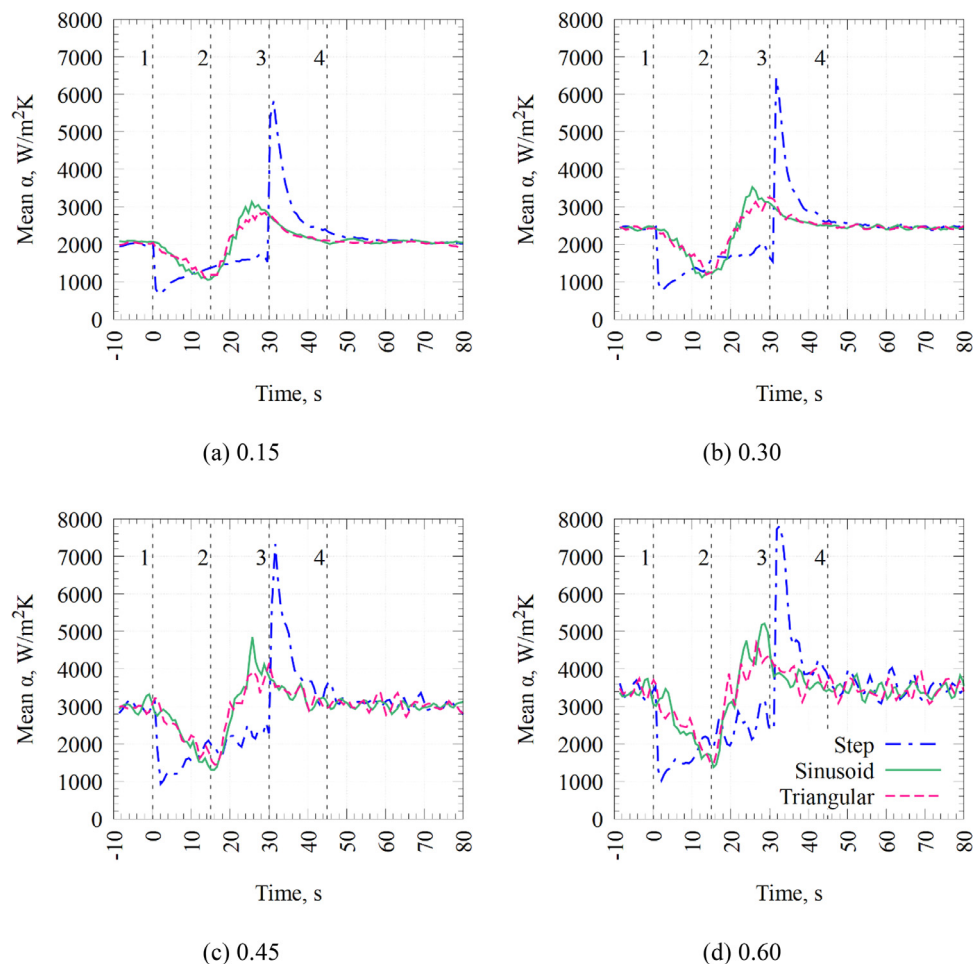


Fig. 10. The mean heat transfer coefficient obtained for four different vapour qualities, indicating qualitatively similar results.

included. For reference, the uncertainty is also shown for these points, being most visible at Point 3 of the step perturbation.

It is evident that for all the perturbation profile cases, significant hysteresis-type effects were present. The average heat transfer coefficient during the first 15 s of the perturbation (Points 1 to 2) was always significantly lower than during the last 15 s (Points 2 to 3) and during the steady-state recovery period (Point 3 to 4), even though the mass flux remained constant. The variation in the heat transfer coefficient was the greatest during the step perturbation profile (blue line). The average heat transfer coefficient from Points 1 to 2 was 1 180 W/m²K, while for Points 2 to 3 and 3 to 4, the coefficients were 1 750 and 3 440 W/m²K respectively. For the sinusoidal and triangular perturbation responses, again appearing relatively similar to each other in Fig. 9 (as was the case in Fig. 8), the average heat transfer coefficients during Periods 1 to 2, 2 to 3, and 3 to 4 were approximately 1 720, 2 700 and 2 640 W/m²K.

Besides for the inlet vapour quality case of 0.30 considered up to this point, similar trends were observed at the other vapour qualities. This is highlighted by the heat transfer coefficient results included in Fig. 10, for vapour qualities of 0.15, 0.30, 0.45, and 0.60.

Although it was not possible to see the behaviour of the actual fluid in the test section itself, certain hypotheses can be made to attempt to explain the decrease in heat transfer coefficient. It is accepted that flow boiling consists of two major contributors: that of convective boiling (affected by the mass flux) and that of nucleate boiling (affected by the heat flux and nucleation sites). Because the mass flow rate remained relatively constant (as is shown later) and the heat flux was changed, it is plausible that the impact of nucle-

ate boiling was the lead cause of the reduction of the heat transfer coefficient. It is possible that the bubble formation (especially for the step perturbation) was curtailed by the decrease, and amplified by the increase. The resolution and frame rate of the outlet sight glass videos was unfortunately too low to capture this behaviour, if it occurred. The outlet sight glass may also have been too far from the heated length, causing any bubbles formed to collapse before being visible.

As mentioned previously, the variation in the heat flux influenced the average vapour quality in the test section during an experiment. Because the heat transfer coefficient was affected by the vapour quality, as shown in Fig. 7, it should be pointed out that the variations in the average heat transfer coefficients (visible in Fig. 8c and Fig. 9) cannot be attributed to the change in the average vapour quality in the test section. At the operating mass flux of 200 kg/m²s, the reference-applied heat flux of 7.5 kW/m² (at approximately Points 1 and 4) resulted in a maximum steady-state vapour quality increase ($\Delta x_{\max} = \frac{Q_{\text{test,max}}}{h_g - h_f}$) over the test section of 0.08 (or 8%). As the applied heat flux changed, the vapour quality difference over the test section also changed, and at the lowest applied heat flux (such as at approximately Point 2), the equivalent minimum steady-state vapour quality increase (Δx_{\min}) over the test section could be expected to be only 0.02 (or 2%). Thus, even though the inlet vapour quality remained constant during an experiment, the average vapour quality in the test section, $x_{\text{ave}} = \frac{1}{2}(x_{\text{in}} + x_{\text{out}})$, was influenced by the applied heat flux. During any experiment (irrespective of the inlet vapour quality), the

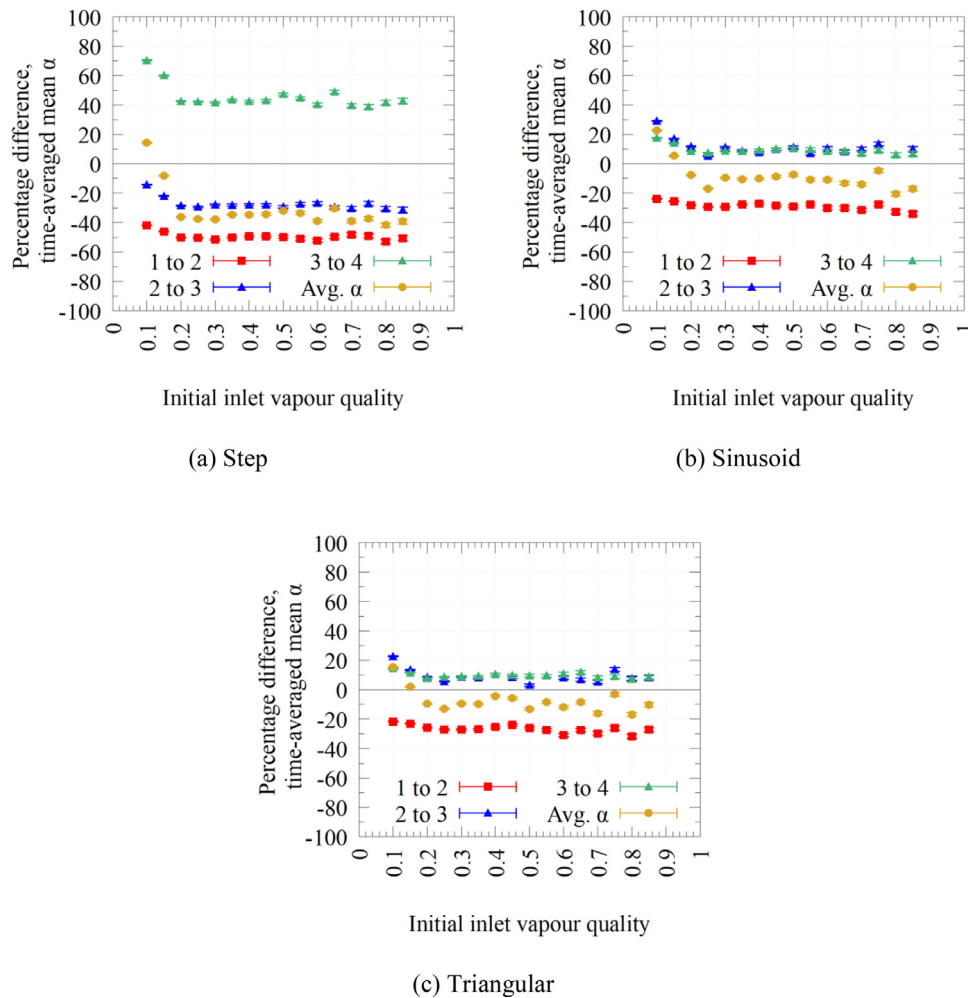


Fig. 11. Maximum average difference in mean heat transfer coefficient for the different stages of the perturbation compared to the steady-state value for all tested qualities for a mass flux of 200 kg/m²s, and an initial heat flux of 7.5 kW/m².

variation of the average vapour quality was at most 0.03 (or 3%), determined as follows: $\Delta x_{ave} = \frac{1}{2}(\Delta x_{max} - \Delta x_{min})$.

When considering the impact of x_{ave} on the average heat transfer coefficient in Fig. 7, we note that a change of 0.03 in x_{ave} will result in a change of only ~90 W/m²K in the heat transfer coefficient. This is based on a first-order linear approximation of data in Fig. 7, which has an average gradient ($\frac{\Delta \alpha}{\Delta x_{ave}}$) of about 3 100 W/m²K from $x = 0$ to $x = 1$. Therefore, the large variations in the heat transfer coefficients during the time span of the perturbation cannot be explained in terms of the vapour quality.

The relevant average heat transfer coefficients for the Periods 1 to 2, 2 to 3, and 3 to 4, as well as the baseline steady-state condition for all flow test cases are tabulated in Table 3 and plotted in Fig. 11.

In the figure, the time-averaged heat transfer coefficient is shown for the time periods discussed before (1 is pre-perturbation, 2 is midway through the perturbation, 3 is at the end of the perturbation, and 4 is 15 s after the perturbation). The step perturbation is shown in Fig. 11a, the sinusoidal perturbation in Fig. 11b, and the ramp triangular perturbation in Fig. 11c. The sum of the average heat transfer coefficient from 1 to 2, 2 to 3, and 3 to 4 is also shown for discussion. This is the total of the average heat transfer coefficient over the entire perturbation (time 1 to 4).

Fig. 11 indicates that, apart from the low vapour qualities of 0.10 and 0.15 (where the flow pattern was not yet fully annular), similar behaviour can be observed for all vapour qualities. The total

average heat transfer coefficient in Fig. 11a is always less than the steady-state value, but the magnitude cannot be compared with the 75% reduction in DNI. The heat transfer coefficient was on average 30% lower than for steady state. For the sinusoidal and triangular perturbations, the total heat transfer coefficients in Fig. 11b and Fig. 11c, were also on average 8% lower than for steady state, in spite of the heat transfer coefficient being momentarily higher than the steady-state heat transfer coefficient between Points 2 and 3 (as indicated in Fig. 8c).

Comparing the triangular perturbation in this study with similar work by Chen et al. [32], many similarities are noted, most notably that their heat transfer coefficient also reached a local minimum at approximately the same time as the applied heat flux, but reached a local maximum appreciably higher than for the steady state before the heat flux had returned to its unperturbed level. They also found that vapour quality had a negligible qualitative effect. However, they found that the time-averaged heat transfer coefficient was not appreciably affected by any amplitude or period of perturbation, while in this study that difference was on average 8%.

The step perturbation can be compared with the work by Wang et al. [34]. Although they tested the commencement of flow boiling from a vapour quality of 0, many similarities can still be seen. The increase in heat flux (as opposed to the strict decrease in this study) showed the opposite behaviour of what was observed in Fig. 8c. The sharp decrease and gradual recovery of the heat trans-

Table 3
Summary of heat transfer coefficient data for all tested inlet vapour qualities and perturbations.

x_{in}	Steady-state heat transfer coefficient (W/m ² K)	Average heat transfer coefficient (W/m ² K)								
		Point 1 to 2			Point 2 to 3			Point 3 to 4		
		Step	Sin.	Triang.	Step	Sin.	Triang.	Step	Sin.	Triang.
0.10	1 890	1 100	1 440	1 480	1 620	2 440	2 320	3 220	2 220	2 160
0.15	2 000	1 080	1 490	1 540	1 560	2 340	2 270	3 200	2 280	2 230
0.20	2 210	1 100	1 590	1 640	1 580	2 470	2 400	3 150	2 400	2 380
0.25	2 320	1 150	1 640	1 690	1 640	2 440	2 450	3 300	2 490	2 520
0.30	2 430	1 180	1 720	1 770	1 750	2 700	2 640	3 440	2 640	2 650
0.35	2 600	1 300	1 880	1 900	1 870	2 830	2 810	3 730	2 820	2 840
0.40	2 770	1 401	2 020	2 070	2 000	2 980	3 060	3 950	3 030	3 060
0.45	2 980	1 510	2 130	2 270	2 150	3 270	3 230	4 260	3 280	3 270
0.50	3 110	1 560	2 210	2 300	2 200	3 460	3 210	4 580	3 430	3 410
0.55	3 260	1 600	2 360	2 370	2 370	3 490	3 570	4 720	3 580	3 570
0.60	3 400	1 620	2 380	2 350	2 490	3 760	3 680	4 770	3 690	3 770
0.65	3 520	1 770	2 460	2 560	2 480	3 810	3 760	5 240	3 830	3 940
0.70	3 730	1 930	2 560	2 620	2 600	4 110	3 930	5 210	4 000	4 040
0.75	3 810	1 940	2 760	2 820	2 780	4 330	4 340	5 290	4 160	4 150
0.80	4 100	1 930	2 760	2 800	2 850	4 350	4 420	5 810	4 350	4 390
0.85	4 330	2 140	2 860	3 150	2 970	4 770	4 690	6 180	4 630	4 710

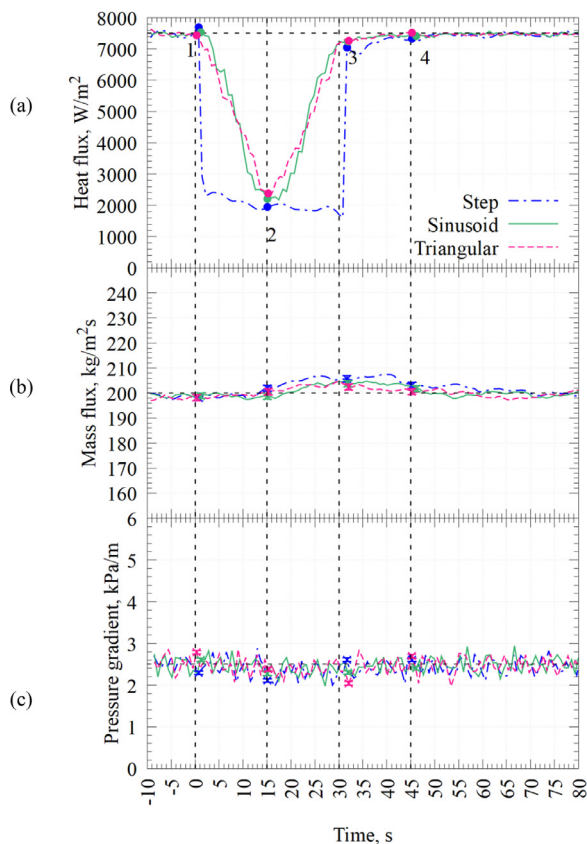


Fig. 12. (a) Step, sinusoidal and triangular heat flux perturbations, and response of (b) mass flux, and (c) pressure drop gradient for a vapour quality of 0.30, mass flux of 200 kg/m²s, and initial heat flux of 7.5 kW/m².

fer coefficient in Fig. 8c is mirrored by an increase and recovery in their work.

Finally, the pressure drop was considered for each perturbation, and no significant differences between the heat flux cases were found to exist. This is illustrated in Fig. 12 for a representative example at a vapour quality of 0.30. Uncertainties are again included at the points of interest. As can be seen, the influence of any pulse perturbation is undetectable. This is understandable, since

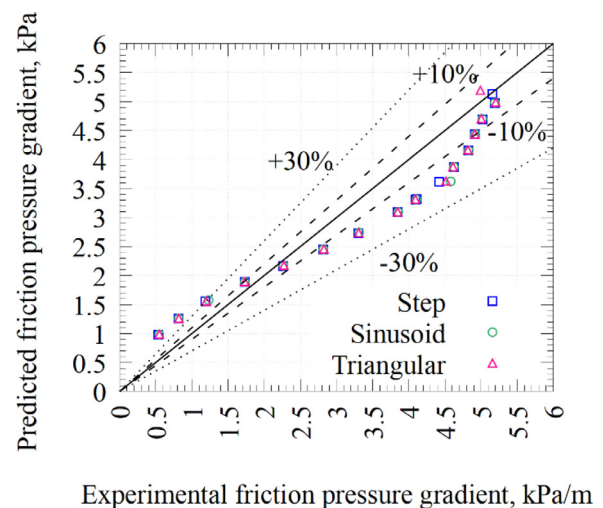


Fig. 13. Frictional pressure drop predicted by the Müller-Steinhagen and Heck correlation compared to the experimental frictional pressure drop.

the change in mass flux and vapour quality was not large enough to significantly impact either the friction or momentum pressure drop. The reason for the mass flux changing almost imperceptibly after a perturbation is due to the closed nature of the system and the fact that the volume and density of the fluid changes with the small vapour quality change.

For interest's sake, the frictional pressure drop gradient, as calculated in Eq. 12, was compared to that predicted by the Müller-Steinhagen and Heck correlation [61] for all vapour qualities considered. This correlation was selected due to its simplicity and robustness. The results are shown in Fig. 13.

The predicted frictional pressure drop for all three perturbations are almost identical, indicating that it was unaffected by the perturbation type. The predictions fall within the expected accuracy for the correlation as has been observed by other authors.

In practical CSP applications, engineers responsible for the design of the solar collector need to take the prevailing weather conditions into account. If large clouds and windy conditions occur regularly, affecting the DNI (as shown in the step perturbation), the expected heat transfer coefficient can be lower by up to 30%. If the cloud cover is relatively sparse and intermittent, the reduction in

heat transfer coefficient will be less, but as shown by the triangular and sinusoidal perturbations, can still be significant. In electronics and battery cooling, this reduction in heat transfer coefficient also needs to be taken into account, and the cooling systems sized appropriately.

4. Further discussion and conclusions

In this paper, we presented results from experimental research into the thermal (and friction) response of two-phase flow boiling to intermittent variations in imposed wall heat flux, motivated by a number of practical and solar DSG applications in particular where any irradiance variation will result in direct heat flux variations on the internal boiling flows.

In particular, the aim of this study was to simulate the effect of partial sub-minute cloud coverage variations on the DNI, with the values and shapes of the perturbations being informed by actual data. The study was conducted in a laboratory set-up especially built for this purpose. Data gathered from this study will inform future experimental and computational work in this space.

Tests were done over inlet vapour qualities ranging from 0.10 to 0.85, at a mass flux of 200 kg/m²s, a base heat flux of 7.5 kW/m², and a saturation temperature of 35°C. Simulated DNI profiles were imposed using a single-pulse perturbation of step, sinusoidal and triangular ramp waveforms. The most important conclusions are as follows:

- All vapour qualities considered showed qualitatively similar results.
- During a step perturbation, the applied heat flux was supplemented visibly by the thermal inertia of the copper pipe.
- Importantly, the heat transfer coefficient did not mirror the applied heat flux, as exhibited by the differing percentages of reduction or increase.
- The sinusoidal and triangular waveforms exhibited almost indistinguishable results.
- During the sinusoidal and triangular perturbations, while the applied heat flux was increasing, the heat transfer coefficient reached a local maximum higher than the unperturbed value before the perturbation was complete.
- The total average heat transfer coefficient was significantly lower during all perturbations than the unperturbed value.
- The change in vapour quality over the test section during the perturbation tests did not account for the change in heat transfer coefficient.
- The pressure drop was unaffected by any perturbation.
- The Müller-Steinhagen and Heck correlation provided acceptable pressure drop predictions.

In closing, it should be noted while the gathered heat transfer coefficient data following the conventional definition based on Newton's law of cooling (Eq. (6)) is useful for practical applications, some questions do arise concerning the usefulness of using this particular definition in unsteady heat transfer problems. For example: Are the extreme values of the heat transfer coefficient when a step change to the heat flux is imposed truly representative of the flow's ability to remove heat from the solid, or just a mathematical artefact due to the formulation of the heat transfer coefficient definition?

In steady-state problems, the conventional heat transfer coefficient definition is a powerful tool in designing thermal systems, however, interpreting heat transfer results through the lens of this definition in an unsteady problem has known limitations, and furthermore, in unsteady problems the simultaneous heat conduction through the solid pipe wall and the convective heat transfer to/from the fluid phase can lead to so-called 'conjugate' heat

transfer phenomena in which the solid itself is actively controlling the thermal performance of the system. Alternative definitions of the heat transfer coefficient were presented and discussed, and the possibility of heat transfer augmentation in a fluid exposed to unsteady conjugate heat transfer was investigated by Mathie and Markides [62], and applied by Mathie et. al [63] who confirmed (and quantified) this experimentally in falling film flows. The complexity concerning the definition, calculation and interpretation (or usefulness) of the heat transfer coefficient that was raised in this work, has also been considered in other studies in the literature. For example, an alternative to using the heat transfer coefficient to predict the wall temperature was also explored by Degiovanni and Remy [64], while the thermal losses associated with conjugate heat transfer in thermal machines were considered by Mathie et. al [65]. This research is ongoing, and until a consensus emerges concerning an improved methodology for characterising and quantifying heat transfer in unsteady flows, the heat transfer coefficient as defined by Newton's law of cooling remains the more common approach used in the literature and in engineering practice. In order to quantify the effect of changing heat flux further, more tests are recommended at different mass fluxes, heat fluxes, and time periods for the perturbations. The results of this study will be useful in the design and sizing of solar collector fields, but are also transferrable to similar applications where flow boiling occurs in the presence of heat flux transients.

Author contributions

Van den Bergh, W.J.: Conceptualisation, methodology, validation, data curation, formal analysis, writing - original draft; **Dirker, J.D.:** Supervision, funding acquisition, formal analysis, writing - review and editing; **Markides, C.N.:** Conceptualisation, funding acquisition, writing - review and editing; **Meyer, J.P.:** Supervision, conceptualisation, funding acquisition, writing - review and editing.

Declaration of Competing Interest

The authors declare that they have no known competing financial interests or personal relationships that could have appeared to influence the work reported in this paper.

Acknowledgements

This work was supported by the Department for International Development (DFID) through the Royal Society-DFID Africa Capacity Building Initiative, and by the UK Engineering and Physical Sciences Research Council (EPSRC) [grant numbers EP/T03338X/1, and EP/P004709/1]. The work was also supported by Russian Government "Megagrant" project 075-15-2019-1888. Data supporting this publication can be obtained on request from cep-lab@imperial.ac.uk.

References

- [1] G. Wang, B. Dong, Z. Chen, Design and behaviour estimate of a novel concentrated solar-driven power and desalination system using S-CO₂ Brayton cycle and MSF technology, *Renewable Energy* 176 (2021) 555–564.
- [2] J. Bundschuh, M. Kaczmarczyk, N. Ghaffour, B. Tomaszewska, State-of-the-art of renewable energy sources used in water desalination: Present and future prospects, *Desalination* 508 (2021) 115035.
- [3] S. Holler, A. Winkelmann, J. Pelda, A. Salaymeh, Feasibility study on solar thermal process heat in the beverage industry, *Energy* 233 (2021) 121153.
- [4] C.N. Markides, The role of pumped and waste heat technologies in a high-efficiency sustainable energy future for the UK, *Applied Thermal Engineering* 53 (2) (2013) 197–209.
- [5] C.N. Markides, Low-concentration solar-power systems based on organic Rankine cycles for distributed-scale applications: Overview and further developments, *Frontiers in Energy Research* 3 (47) (2015).

- [6] Z.A. Smith, K.D. Taylor, *Renewable and Alternative Energy Resources: A Reference Handbook*, ABC-CLIO, 2008.
- [7] W. Fuqiang, C. Ziming, T. Jianyu, Y. Yuan, S. Yong, L. Linhua, Progress in concentrated solar power technology with parabolic trough collector system: A comprehensive review, *Renewable and Sustainable Energy Reviews* 79 (2017) 1314–1328.
- [8] H.L. Zhang, J. Baeyens, J. Degrève, G. Caçères, Concentrated solar power plants: Review and design methodology, *Renewable and Sustainable Energy Reviews* 22 (2013) 466–481.
- [9] R.K. Pal, R.K. K, Investigations of thermo-hydrodynamics, structural stability, and thermal energy storage for direct steam generation in parabolic trough solar collector: A comprehensive review, *Journal of Cleaner Production* 311 (2021) 127550.
- [10] A. Fernández-García, E. Zarza, L. Valenzuela, M. Pérez, Parabolic-trough solar collectors and their applications, *Renewable and Sustainable Energy Reviews* 14 (7) (2010) 1695–1721.
- [11] A. Sharma, A.K. Shukla, O. Singh, M. Sharma, Recent advances in gas/steam power cycles for concentrating solar power, *International Journal of Ambient Energy* (2021) 1–12.
- [12] J. Dirker, D. Juggurnath, A. Kaya, E. Osowade, M. Simpson, S. Lecompte, S.M.A. Noori Rahim Abadi, V. Voulgaropoulos, A. Adelaja, M. Dauhoo, A. Khoodaruth, S. Obayopo, O. Olakoyejo, M. Khalil, M. De Paepe, J. Meyer, C. Markides, Thermal energy processes in direct steam generation solar systems: Boiling, condensation and energy storage – A review, *Frontiers in Energy Research* (2018).
- [13] J. Freeman, K. Hellgardt, C.N. Markides, Working fluid selection and electrical performance optimisation of a domestic solar-ORC combined heat and power system for year-round operation in the UK, *Applied Energy* 186 (2017) 291–303.
- [14] J. Freeman, K. Hellgardt, C.N. Markides, An assessment of solar-powered organic Rankine cycle systems for combined heating and power in UK domestic applications, *Applied Energy* 138 (2015) 605–620.
- [15] A.M. Pantaleo, S.M. Camporeale, A. Sorrentino, A. Miliuzzi, N. Shah, C.N. Markides, Hybrid solar-biomass combined Brayton/organic Rankine-cycle plants integrated with thermal storage: Techno-economic feasibility in selected Mediterranean areas, *Renewable Energy* 147 (2020) 2913–2931.
- [16] Z. Ye, J. Yang, J. Shi, J. Chen, Thermo-economic and environmental analysis of various low-GWP refrigerants in organic Rankine cycle system, *Energy* 199 (2020) 117344.
- [17] Y. Feng, T. Hung, Y. Zhang, B. Li, J. Yang, Y. Shi, Performance comparison of low-grade ORCs (organic Rankine cycles) using R-245fa, pentane and their mixtures based on the thermoeconomic multi-objective optimization and decision makings, *Energy* 93 (2015) 2018–2029.
- [18] R. Rayegan, Y.X. Tao, A procedure to select working fluids for solar organic Rankine cycles (ORCs), *Renewable Energy* 36 (2) (2011) 659–670.
- [19] T.C. Roumpedakis, G. Loumpardis, E. Monokrousou, K. Braimakis, A. Charalampidis, S. Karellas, Exergetic and economic analysis of a solar driven small scale ORC, *Renewable Energy* 157 (2020) 1008–1024.
- [20] S.H. Kang, Design and experimental study of ORC (organic Rankine cycle) and radial turbine using R-245fa working fluid, *Energy* 41 (1) (2012) 514–524.
- [21] J. Kajurek, A. Rusowicz, A. Grzebielec, W. Bujalski, K. Futyma, Z. Rudowicz, Selection of refrigerants for a modified organic Rankine cycle, *Energy* 168 (2019) 1–8.
- [22] R. Daghigh, A. Shafieian, An investigation of heat recovery of submarine diesel engines for combined cooling, heating and power systems, *Energy Conversion and Management* 108 (2016) 50–59.
- [23] B. Xu, D. Rathod, A. Yebi, Z. Filipi, S. Onori, M. Hoffman, A comprehensive review of organic Rankine cycle waste heat recovery systems in heavy-duty diesel engine applications, *Renewable and Sustainable Energy Reviews* 107 (2019) 145–170.
- [24] T. Zhang, E.N. Wang, Design of a microscale organic Rankine cycle for high-concentration photovoltaics waste thermal power generation, 13th InterSociety Conference on Thermal and Thermomechanical Phenomena in Electronic Systems, 2012.
- [25] P.R. Parida, T. Chainer, Numerical investigation of coolants for chip-embedded two-phase cooling, 2020 36th Semiconductor Thermal Measurement, Modeling & Management Symposium (SEMI-THERM), 2020.
- [26] Y. Chu, H.T.C. Pedro, M. Li, C.F.M. Coimbra, Real-time forecasting of solar irradiance rams with smart image processing, *Solar Energy* 114 (2015) 91–104.
- [27] H. Ait Lahoussine Ouali, R. Guechchati, M.A. Moussaoui, A. Mezrhah, Performance of parabolic through solar power plant under weather conditions of the Oujda city in Morocco, *Applied Solar Energy* 53 (1) (2017) 45–52.
- [28] J.F. Feldhoff, T. Hirsch, An approach to DNI transients characterization for system evaluation, *AIP Conference Proceedings* 1850 (1) (2017) 160007.
- [29] M. Eck, T. Hirsch, Dynamics and control of parabolic trough collector loops with direct steam generation, *Solar Energy* 81 (2) (2007) 268–279.
- [30] D. Wang, L. Zhao, X. Nie, Y. Lu, S. Deng, Experimental study on flow boiling characteristics of R-245fa in circular tube under non-uniform heat flux, *International Journal of Heat and Mass Transfer* 143 (2019) 118570.
- [31] C. Chen, W. Chang, T. Lin, Time periodic flow boiling heat transfer of R-134a and associated bubble characteristics in a narrow annular duct due to flow rate oscillation, *International Journal of Heat and Mass Transfer* 53 (19) (2010) 3593–3606.
- [32] C.A. Chen, T.F. Lin, W.-M. Yan, Experimental study on time periodic evaporation heat transfer of R-134a in annular ducts due to wall heat flux oscillation, *International Journal of Heat and Mass Transfer* 106 (2017) 1232–1241.
- [33] I.W. Park, J. Ryu, M. Fernandino, C.A. Dorao, Can flow oscillations during flow boiling deteriorate the heat transfer coefficient? *Applied Physics Letters* 113 (15) (2018) 154102.
- [34] S.L. Wang, C.A. Chen, Y.L. Lin, T.F. Lin, Transient oscillatory saturated flow boiling heat transfer and associated bubble characteristics of FC-72 over a small heated plate due to heat flux oscillation, *International Journal of Heat and Mass Transfer* 55 (4) (2012) 864–873.
- [35] R. Mahoney, Trough technology heat collector element (HCE) solar selective absorbers, Trough Workshop ASES 2000m, 2000.
- [36] D. Lei, Z. Wang, J. Li, The analysis of residual stress in glass-to-metal seals for solar receiver tube, *Materials & Design* 31 (4) (2010) 1813–1820.
- [37] O. Shekoofa, J. Wang, J. Qi, J. Zhang, Z. Yin, Analysis of residual stress for mismatch metal-glass seals in solar evacuated tubes, *Solar Energy Materials and Solar Cells* 128 (2014) 421–426.
- [38] M.H. Abedini-Sanigy, F. Ahmadi, E. Goshtasbirad, M. Yaghoubi, Thermal stress analysis of absorber tube for a parabolic collector under quasi-steady state condition, *Energy Procedia* 69 (2015) 3–13.
- [39] W. Fuqiang, T. Jianyu, M. Lanxin, W. Chengchao, Effects of glass cover on heat flux distribution for tube receiver with parabolic trough collector system, *Energy Conversion and Management* 90 (2015) 47–52.
- [40] V. Flores, R. Almanza, Behavior of the compound wall copper-steel receiver with stratified two-phase flow regimen in transient states when solar irradiance is arriving on one side of receiver, *Solar Energy* 76 (1) (2004) 195–198.
- [41] F. Wang, Y. Shuai, Y. Yuan, G. Yang, H. Tan, Thermal stress analysis of eccentric tube receiver using concentrated solar radiation, *Solar Energy* 84 (10) (2010) 1809–1815.
- [42] J. Dirker, W.J. Van den Bergh, H.R. Moran, C.N. Markides, J.P. Meyer, Influence of inlet vapour quality perturbations on the transient response of flow-boiling heat transfer, *International Journal of Heat and Mass Transfer* 170 (2021) 121017.
- [43] J. Freeman, I. Guarracino, S.A. Kalogirou, C.N. Markides, A small-scale solar organic Rankine cycle combined heat and power system with integrated thermal energy storage, *Applied Thermal Engineering* 127 (2017) 1543–1554.
- [44] A. Ramos, M.A. Chatzopoulou, J. Freeman, C.N. Markides, Optimisation of a high-efficiency solar-driven organic Rankine cycle for applications in the built environment, *Applied Energy* 228 (2018) 755–765.
- [45] B.-S. Park, M. Usman, M. Imran, A. Pesyridis, Review of organic Rankine cycle experimental data trends, *Energy Conversion and Management* 173 (2018) 679–691.
- [46] Armacell. HVAC-R & Process Specification Guide. 2021; Available from: <https://local.armacell.com/fileadmin/cms/uk/service/en/ArmaflexUKSpecGuideDigital.pdf>.
- [47] S.G. Kandlikar, W.J. Grande, Evolution of microchannel flow passages: thermo-hydraulic performance and fabrication technology, *Heat Transfer Engineering* 24 (1) (2003) 3–17.
- [48] K. Cho, S.-J. Tae, Condensation heat transfer for R-22 and R-407C refrigerant-oil mixtures in a microfin tube with a U-bend, *International Journal of Heat and Mass Transfer* 44 (11) (2001) 2043–2051.
- [49] I.H. Bell, J. Wronski, S. Quoilin, V. Lemort, Pure and pseudo-pure fluid thermophysical property evaluation and the open-source thermophysical property library CoolProp, *Industrial & Engineering Chemistry Research* 53 (6) (2014) 2498–2508.
- [50] L. Wojtan, T. Ursenbacher, J.R. Thome, Investigation of flow boiling in horizontal tubes: Part I—A new diabatic two-phase flow pattern map, *International Journal of Heat and Mass Transfer* 48 (14) (2005) 2955–2969.
- [51] Y.A. Cengel, Heat and mass transfer: a practical approach: SI units, McGraw-Hill, Singapore, 2006.
- [52] J. Moreno Quibén, J.R. Thome, Flow pattern based two-phase frictional pressure drop model for horizontal tubes. Part I: Diabatic and adiabatic experimental study, *International Journal of Heat and Fluid Flow* 28 (5) (2007) 1049–1059.
- [53] D. Steiner, Heat Transfer to Boiling Saturated Liquids (VDI-Wärmeatlas). VDI Heat Atlas. VDI-Gesellschaft Verfahrenstechnik und Chemieingenieurwesen (GCV), Düsseldorf, Germany, 1993 (JW Fullarton, translator).
- [54] S.Z. Rouhani, E. Axelsson, Calculation of void volume fraction in the subcooled and quality boiling regions, *International Journal of Heat and Mass Transfer* 13 (2) (1970) 383–393.
- [55] Dunn, P.F. and Davis, M.P., *Measurement and data analysis for engineering and science*, 2018.
- [56] V. Gnielinski, New equations for heat and mass transfer in turbulent pipe and channel flow, *Int. Chem. Eng.* 16 (2) (1976) 359–368.
- [57] J.P. Meyer, M. Everts, N. Coetzee, K. Grote, M. Steyn, Heat transfer coefficients of laminar, transitional, quasi-turbulent and turbulent flow in circular tubes, *International Communications in Heat and Mass Transfer* 105 (2019) 84–106.
- [58] L. Wojtan, T. Ursenbacher, J.R. Thome, Investigation of flow boiling in horizontal tubes: Part II—Development of a new heat transfer model for stratified-wavy, dryout and mist flow regimes, *International Journal of Heat and Mass Transfer* 48 (14) (2005) 2970–2985.
- [59] X. Fang, Q. Wu, Y. Yuan, A general correlation for saturated flow boiling heat transfer in channels of various sizes and flow directions, *International Journal of Heat and Mass Transfer* 107 (2017) 972–981.
- [60] K.E. Gungor, R.H.S. Winterton, A general correlation for flow boiling in tubes and annuli, *International Journal of Heat and Mass Transfer* 29 (3) (1986) 351–358.

- [61] H. Müller-Steinhagen, K. Heck, A simple friction pressure drop correlation for two-phase flow in pipes, *Chemical Engineering and Processing: Process Intensification* 20 (6) (1986) 297–308.
- [62] R. Mathie, C.N. Markides, Heat transfer augmentation in unsteady conjugate thermal systems – Part I: Semi-analytical 1-D framework, *International Journal of Heat and Mass Transfer* 56 (1) (2013) 802–818.
- [63] R. Mathie, H. Nakamura, C.N. Markides, Heat transfer augmentation in unsteady conjugate thermal systems – Part II: Applications, *International Journal of Heat and Mass Transfer* 56 (1) (2013) 819–833.
- [64] A. Degiovanni, B. Remy, An alternative to heat transfer coefficient: A relevant model of heat transfer between a developed fluid flow and a non-isothermal wall in the transient regime, *International Journal of Thermal Sciences* 102 (2016) 62–77.
- [65] R. Mathie, C.N. Markides, A.J. White, A framework for the analysis of thermal losses in reciprocating compressors and expanders, *Heat Transfer Engineering* 35 (16-17) (2014) 1435–1449.